Nanoscale

Dual Contrast Agents for Fluorescence and Photoacoustic Imaging: Evaluation in a Murine Model of Prostate Cancer

Journal:	*Nanoscale*
Manuscript ID	NR-ART-01-2021-000669.R1
Article Type:	Paper
Date Submitted by the Author:	17-Apr-2021

Complete List of Authors:	Lesniak, Wojtek ; Johns Hopkins Medical Institutions Campus Yu, Yixuan; Johns Hopkins Medical Institutions Kang, Jeeun; Johns Hopkins University, ; Boinapally, Srikanth; Johns Hopkins School of Medicine, Department of Radiology Ray Banerjee, Sangeeta; Johns Hopkins University, Radiology Lisok, Ala; Johns Hopkins Medical Institutions Jabolonska, Anna; Johns Hopkins Medical Institutions Boctor, Emad; Johns Hopkins Medical Institutions Pomper, MG; Johns Hopkins Medical Institutions,

ARTICLE

Received 00th January 20xx,

Accepted 00th January 20xx

DOI: 10.1039/x0xx00000x

Dual Contrast Agents for Fluorescence and Photoacoustic Imaging: Evaluation in a Murine Model of Prostate Cancer

Wojciech G. Lesniak[a*], Yixuan Wu[b,c*], Jeeun Kang[a,c], Srikanth Boinapally[a], Sangeeta Ray Banerjee[a], Ala Lisok[a], Anna Jablonska[a,d], Emad M. Boctor[a,b,c,e**] and Martin G. Pomper[a**]

Prostate-specific membrane antigen (PSMA) is a promising diagnostic and therapeutic target for prostate cancer (PC). Poly(amidoamine) [PAMAM] dendrimers serve as versatile scaffolds for imaging agents and drug delivery that can be tailored to different sizes and compositions depending upon the application. We have developed PSMA-targeted PAMAM dendrimers for real-time detection of PC using fluorescence (FL) and photoacoustic (PA) imaging. A generation-4, ethylenediamine core, amine-terminated dendrimer was consecutively conjugated with on average 10 lysine-glutamate-urea PSMA targeting moieties and a different number of sulfo-cyanine7.5 (Cy7.5) near-infrared dyes (2, 4, 6 and 8 denoted as conjugates II, III, IV and V, respectively). The remaining terminal primary amines were capped with butane-1,2-diol functionalities. We also prepared a conjugate composed of Cy7.5-lysine-suberic acid-lysine glutamate-urea (I) and control dendrimer conjugate (VI). Among all conjugates, IV showed superior *in vivo* target specificity in male NOD-SCID mice bearing isogenic PSMA$^+$ PC3 PIP and PSMA$^-$ PC3 flu xenografts and suitable physicochemical properties for FL and PA imaging. Such agents may prove useful in PC cancer detection and subsequent surgical guidance during excision of PSMA-expressing lesions.

[a]Russell H. Morgan Department of Radiology and Radiological Science; [b]Department of Computer Science; [c]Laboratory for Computational Sensing and Robotics; [d]Institute for Cell Engineering; [f]Department of Electrical and Computer Engineering, Johns Hopkins University, Baltimore, MD 21218, USA

*These authors contributed equally to this work.

**Correspondence authors:

Email:mpomper@jhmi.edu

Email: eboctor1@jhmi.edu

Electronic Supplementary Information (ESI) available: [details of any supplementary information available should be included here]. See DOI: 10.1039/x0xx00000x

1. Introduction

Prostate cancer (PC) is the second most common malignancy in men and the fifth leading cause of cancer-related death, with more than 1.1 million new cases diagnosed annually worldwide.[1] There is a consensus that early detection of aggressive PC and selection of optimal treatment would increase the rate of cure.[2-4] Prostate-specific antigen (PSA) testing and serial prostate biopsies are widely utilized for active surveillance of PC.[5, 6] While elevated blood levels of PSA allow early PC detection, recent studies indicate that its utility for guiding treatment may be lacking.[7] An elevated PSA level may rather suggest performance of a more informative or definitive procedure, such as ultrasound-guided transrectal or transperineal needle biopsy. However, those procedures are likewise limited due to sampling error as well as possible side effects, such as pain, bleeding and infection.[8] Accordingly, in the early phases of management, patients with PC may have incomplete characterization of their tumor, which may lead to inappropriate management.[2-4] There is an urgent need for development of more accurate and less invasive methods for active surveillance of, and when necessary, surgical guidance for patients with PC.

Molecular and functional imaging provide another layer of precision in the detection, treatment planning and therapeutic monitoring of PC. To that end, non-invasive imaging of prostate-specific membrane antigen (PSMA) expression is being evaluated extensively, as it is overexpressed in most PCs, and has been associated with androgen-independent and aggressive disease.[9-11] The level of PSMA expression correlates well with elevated PSA and Gleason score and can be utilized for PC staging.[12] PSMA expression in cancers has been imaged with low-molecular-weight agents, monoclonal antibodies and nanoparticles using different types of imaging modalities including radionuclide, magnetic resonance and optical imaging.[13-17]

Photoacoustic (PA) imaging is a biomedical imaging modality that combines the superior molecular contrast and specificity of optical imaging with the sub-micrometer spatial resolution and centimeter-scale imaging depth of ultrasound (US).[18-21] PA imaging is a compact, cost-effective, non-radiative, and minimally invasive modality, with the ability to detect hemoglobin, lipids, water and other light-absorbing chromophores, providing functional and molecular information that enable a wide range of pre-clinical and clinical applications. PA imaging yields better specificity and depth of penetration than possible with conventional US and optical imaging, respectively.[20, 22] A number of contrast agents for PA imaging have been developed and extensively evaluated for biomedical purposes, including gold nanocrystals, graphene-based agents, carbon nanotubes, organic nanoparticles, and semiconducting polymeric nanoparticles.[19, 23, 24] An ideal PA contrast agent should exhibit low quantum yield, high molar extinction coefficient, a near-infrared (NIR) absorption window, photostability, biocompatibility, and high target specificity.

We have recently demonstrated that PSMA expression can be assessed *in vivo* with PA imaging using a commercially available near-infrared optical imaging agent, YC-27, composed of a lysine-glutamate-urea (KEU) PSMA inhibitor, linker (lysine-suberic acid) and the IRDye 800CW fluorophore (YC-27).[25] However, YC-27 does not allow systematic exploration of photoacoustic enhancement, nor can it be used for phototherapy. In contrast, because of their highly tunable properties, poly(amidoamine) [PAMAM] dendrimers may add another dimension to PA imaging, specifically the ability to deliver multiple modalities at once, including imaging and therapeutic moieties.[26] PAMAM dendrimers are well-defined scaffolds with low polydispersity, many reactive terminal groups, a large interior void volume, flexibility, biocompatibility and the capacity for straightforward modification. Accordingly, PAMAM dendrimers have been used as nanomaterials for various biomedical applications including targeted drug delivery, gene transfection of cells and biomedical imaging.[26, 27] We recently demonstrated that generation-4 PAMAM dendrimers conjugated with the KEU PSMA-targeting moieties showed superior uptake within $PSMA^+$ PC3 PIP tumors vs. $PSMA^-$ PC3 flu tumors with low uptake in off-target tissues.[28] The pharmacokinetics of these dendrimers indicate that they may be used for targeting PSMA-expressing tissues for cancer imaging or therapy. Here we present a proof-of-concept study showing that PAMAM dendrimer-based nanoplatforms can provide FL and PA contrast for PC detection, with potential for further development of related theranostic agents. The framework described presents a mechanism of PA signal amplification for maximal imaging sensitivity, based on fluorescence quenching and a multi-scaffold dye configuration.

2. Materials and methods

2.1. Materials

Chemicals were purchased from Sigma-Aldrich or Fisher Scientific unless otherwise specified. Ethylenediamine core amine-terminated generation-4 poly(amidoamine) dendrimer $G4(NH_2)_{64}$ was acquired from Dendritech (Midland, MI). Sulfo-Cyanine7.5 NHS ester (Cy7.5-NHS) and *N*-[[[(1*S*)-1-carboxy-3-methylbutyl]amino]carbonyl]-L-glutamic acid (ZJ-43) was purchased from Lumirpobe Life science solutions (Hunt Valley, MD) and Tocris Bioscience (Minneapolis, MN), respectively. L-Glutamic acid di-*tert*-butyl ester hydrochloride, N^{ε}-Z-L-lysine *tert*-butyl ester hydrochloride and N^{ε}-Boc-L-lysine were purchased from Chem-Impex International, Inc (Wood Dale, IL). Disuccinimidyl suberate was acquired from TCI America (Montgomeryville, PA). All reagents and solvents were used as received without further purification.

2.2. Synthesis

Di-tert-butyl(((S)-1-(tert-butoxy)-6-(8-((2,5-dioxopyrrolidin-1-yl)oxy)-8-oxooctanamido) 1oxohexan-2-yl) carbamoyl)-L-glutamate (1): The protected lysine-glutamate-urea (KEU) was synthetized as we have previously reported.[29] To the stirred solution of dimethylformamide (DMF, 7 mL) containing disuccinimidyl suberate (DSS, 415 mg, 1.12 mmol, 2.2 mol equivalent) was added 3 mL of DMF containing protected KEU (250 mg, 0.513 mmol, 1.0 mol equivalent) and triethylamine (71 µL, 0.513 mmol, 1.0 mol equivalent) dropwise for 20 min under a nitrogen atmosphere at room temperature (RT). The resulting mixture was stirred for an additional 2 h at RT, followed by concentration under reduced pressure at 40°C. Crude product was purified by silica column chromatography using acetonitrile and dichloromethane as eluents (40% acetonitrile in dichloromethane) to afford **1** as a viscous liquid (228 mg, yield 60%). ^{1}H NMR ($CDCl_3$): 6.30 (t, J = 5.5 Hz, 1H), 5.45 (dd, J = 8.0, 18.5 Hz, 2H), 4.35 (m, 2H), 3.15-3.35 (m, 2H), 2.82 (s, 4H), 2.65 (t, J = 7.0 Hz, 2H), 2.41 (m, 2H), 2.20 (t, J = 7.0 Hz, 2H), 2.18-1.21 (m, 43H); ESI-MS m/z: 741.4 [M+H]. Subsequently, 200 mg (0.27 mmol) of **1** was dissolved in a solution composed of 2 mL of trifluoroacetic acid (TFA) and 2 mL of dichloromethane (DCM), with the resulting mixture stirred at RT for 2 h, followed by drying in *vacuo.* The crude product was purified by reverse-phase (RP) flash chromatography using 0.1% TFA in H_2O (A) and 0.1% TFA in acetonitrile (B) as eluents, followed by lyophilization, which afforded NHS-SA-KEU in 90% yield (139 mg). Flash chromatography was carried out using a Biotage Isolera One system (Biotage Sweden AB, Cardiff, UK) with the detection wavelength set to 220 nm, Biotage SNAP Ultra C18 column (12 g) and gradient elution starting with 90% A and 10% B, reaching 90% B. The desired product eluted with the 50% B to 55% A. ^{1}H-NMR (500 MHz, CD_3OD): δ 4.33-4.23 (m, 2H), 3.17 (t, J = 7.0 Hz, 2H), 2.83 (s, 4H), 2.62 (t, J = 7.5 Hz, 2H), 2.46-2.33 (m, 2H), 2.21-2.09 (m, 3H), 1.92-1.59 (m, 7H), 1.55-1.33 (m, 8H); ESI-MS m/z: 573.2 [M+H].

(3S,7S,22S)-26-Amino-5,13,20-trioxo-4,6,12,21-tetraazahexacosane-1,3,7,22-tetracarboxylic acid (2): 70 mg of **1** (0.094 mmol, 1.0 mol equivalent) and 27.9 mg of N^{ε}-Boc-L-Lysine (0.113 mmol, 1.2 mol equivalent) were dissolved in 500 µL of dimethyl sulfoxide (DMSO) and 49 µL of diisopropylethylamine (DIPEA, 0.283 mmol, 3.0 mol equivalent) was added. The resulting mixture was stirred for 2 h at RT and concentrated *in vacuo* to afford a thick residue. This residue was dissolved in a solution containing 2 mL of TFA and 2 mL of DCM and stirred for 2 h at RT, followed by concentrated in *vacuo.* The crude product was purified by RP flash chromatography using 0.1% TFA in H_2O (A) and 0.1% TFA in acetonitrile (B) as eluents, followed by lyophilization, which provided K-SA-KEU as a colorless solid in 80% yield (45 mg). Purification by flash chromatography was achieved using the Biotage Isolera One system, λ 220 nm, Biotage SNAP Ultra C18 column (12 g), solvent gradient: 90% A and 10% B, reaching 90% B. The desired product eluted with the fraction at 40% to 45% of B in A. ^{1}H-NMR (500 MHz, CD_3OD): δ 4.44-4.37 (m, 1H), 4.34-4.22 (m, 2H), 3.17 (t, J = 5.5 Hz, 2H), 2.95-2.88 (m, 2H), 2.45-2.37 (m, 2H), 2.25 (t, J = 7.0 Hz, 2H), 2.17 (t, J = 7.5 Hz, 2H), 1.97-1.79 (m, 4H), 1.77-1.26 (m, 18H); ESI-MS m/z: 604.3 [M+H].

*1,1-Dimethyl-3-((3S,7S,22S)-1,3,7,22-tetracarboxy-5,13,20,28-tetraoxo-4,6,12,21,27-pentaazatritriacontan-33-yl)-2-((E)-2-((E)-3-((E)-2-(1,1,3-trimethyl-6,8-disulfonato-1,3-dihydro-2H-benzo[e]indol-2-ylidene)ethylidene)cyclohex-1-en-1-yl)vinyl)-1H-benzoindol-3-ium-6,8-disulfonate (Conjugate **I** - Cy7.5-K-SA-KEU):* To a stirred solution of DMSO (20 µL) containing K-SA-KEU (3.83 mg, 63 µmol, 1.5 mol equivalent) and sulfo-Cy7.5-NHS ester (5 mg, 42 µmol, 1.0 mol equivalent) 8.8 µL of DIPEA (50 µmol, 12 mol equivalent) was added. The reaction mixture was stirred for 2 h at RT and concentrated *in vacuo*, which afforded a thick green residue. The crude product was dissolved in deionized water and purified using a Varian ProStar high performance liquid chromatography (HPLC) pumps connected to a semi-preparative C-18 Luna column (5 µm, 10×250 mm, Phenomenex) and an Agilent 1260 Infinity photodiode array detector. A gradient elution starting with 98% aqueous 20 mM triethyl ammonium acetate buffer (A) and 2% acetonitrile (B), reaching 100% of B in 30 min at a flow rate of 4 mL/min was applied. The product was collected between 11.5 and 12.5 min of elution, followed by evaporation on a rotary evaporator. Lyophilization afforded Cy7.5-K-SA-KEU conjugate **I** as a dark green solid (1.8 mg, yield 70%).

Synthesis of dendrimer conjugates. All dendrimer conjugates were synthesized using a one-pot approach we recently reported.[28] In a typical reaction, 10 mg of $G4(NH_2)_{64}$ (0.7 µmol) dissolved in 2 mL of PBS mixed with 100 µL of DMSO containing 1.66 mg (1.41 µmol, for conjugate **II**) or 3.72 mg (3.15 µmol, for conjugate **III**) or 5.81 mg (4.92 µmol, for conjugate **IV** and **VI**) or 10 mg (8.44 µmol, for conjugate **V**) of Cy7.5-NHS. After 2 h of stirring at RT an aliquot of each reaction mixture was subjected to matrix-assisted laser desorption/ionization-time-of-flight (MALDI-TOF) mass spectrometry (MS) to assess the number of Cy7.5 dyes conjugated with dendrimer. Next, 5 mg (9.58 µmol) of NHS-SA-KEU dissolved in 100 µL of DMSO was added to each reaction mixture and reacted for 2 h, followed by MADLI-TOF mass spectrometry to confirm covalent attachment of SA-KEU with $G4(NH_2)_{62}(Cy7.5)_2$, $G4(NH_2)_{60}(Cy7.5)_4$, $G4(NH_2)_{58}(Cy7.5)_6$ and $G4(NH_2)_{56}(Cy7.5)_8$ conjugates. In the final synthetic step, 0.2 mL (3 mmol) of glycidol was added to each reaction mixture, which was stirred overnight at RT to cap the remaining unmodified primary amines with butane-1,2-diol. The non-targeted control dendrimer was formulated by reacting $G4(NH_2)_{64}$ dendrimer with 5.81 mg (4.92 µmol) of Cy7.5 dye and 0.2 mL (3 mmol) of glycidol. Resulting conjugates **II** $[G4(NH_2)_{20}(Cy7.5)_2(SA\text{-}KEU)_{10}(Bdiol)_{32}]$, **III** $[G4(NH_2)_{21}(Cy7.5)_4(SA\text{-}KEU)_9(Bdiol)_{30}]$, **IV** $[G4(Cy7.5)_6(SA\text{-}KEU)_9(Bdiol)_{53}]$, **V** $[G4(Cy7.5)_8(SA\text{-}KEU)_{12}(Bdiol)_{52}]$ and **VI** $[G4(NH_2)_{13}(Cy7.5)_6(Bdiol)_{45}]$ were purified using Amicon

centrifugal filters with 10,000 Da MWCO (Millipore Sigma, Rockville, MD) and deionized water, followed by lyophilization and characterization by RP-HPLC, MALDI-TOF MS, UV-Vis and FL spectroscopy.

2.3. Characterization

RP-HPLC. Analysis was carried out using Varian ProStar system equipped with a 1260 Infinity photodiode array detector (Agilent) and a semi-preparative C-18 Luna column (5 mm, 10×25 mm Phenomenex) and gradient elution. The gradient proceeded as: 98% H_2O (0.1% TFA) and 2% acetonitrile (0.1% TFA), reaching 100% of acetonitrile (0.1% TFA) in 30 min at a flow rate of 4 mL/min.

MALDI-TOF MS. Spectra of $G4(NH_2)_{64}$, intermediate conjugates, and final conjugates were recorded on a Voyager DE-STR spectrometer (Norwalk, CT). 2,5-dihydroxybenzoic acid (DHB) matrix was dissolved in 50% MeOH and 0.1% TFA aqueous solution at 20 mg/mL. Conjugates obtained from the reaction mixture were passed through Zeba Spin desalting columns at a 7,000 Da MWCO (ThermoFisher Scientific, Waltham, MA). 10 µL of matrix solution was mixed with 10 µL of solutions containing conjugates. Next, 1 µL of the resulting mixture was placed on the target plate and evaporated. The number of shots and laser power were adjusted according to spectrum quality.

Dynamic light scattering and zeta potential

Dynamic light scattering and zeta potential analyses were performed using a Malvern Zetasizer Nano ZEN3600. Results are presented as a mean of three sequential measurements. All the analyzed conjugates were prepared at a concentration of 2 mg/ml in PBS (c= 0.01M, pH 7.4). Measurements were performed at 25°C.

Near-infrared (NIR) spectrophotometry and spectrofluorometry. Spectrophotometric and spectrofluorometric properties of all conjugates were measured on a SpectraMax i3x multi-mode system (Molecular Devices, LLC, San Jose, CA). The Costar clear and black polystyrene 96-well microplates were used for UV-vis spectrophotometry and spectrofluorometry, respectively, and the reading positions were automatically optimized by SpectraMax i3x. All data were acquired under the same settings, the temperature of all measurements was kept at 20°C, and the volume of all evaluated samples was 200 µL, which contained 0.96 nmol sulfo-Cy7.5 NIR dye. The NIR optical absorbance characteristics of the conjugates were acquired in the range of 650 nm to 950 nm in steps of 1 nm. FL excitation was at 715 nm and the emission was from 750 nm to 850 nm in steps of 1 nm with 100 flashes per recording.

Cell lines and tumor models. $PSMA^+$ PC3 PIP (high PSMA expression) and $PSMA^-$ PC3 flu (low PSMA expression) cell lines were originally obtained from Dr. Warren Heston (Cleveland Clinic, OH) and were maintained as previously described.[30] Cells were grown to 80%-90% confluence before trypsinization and formulation in Hank's balanced salt solution (HBSS, Sigma) for inoculation into mice. All animal procedures were performed in accordance with United States Public Health Service Policy on the Humane Care and Use of Laboratory Animals, and approved by the Johns Hopkins University Animal Care and Use Committee (ACUC, MO18M97).

For FL and PA imaging intact male NOD-SCID mice (Johns Hopkins University, in-house colony) were inoculated subcutaneously in the lower back near the left and right posterior flanks with 1×10^6 $PSMA^+$ PC3 PIP and $PSMA^-$ PC3 flu cells. $PSMA^+$ PC3 PIP and $PSMA^-$ PC3 flu tumors grew next to each other to enable side-by-side FL and PA imaging. Mice were shaved and imaged when the tumors reached 2.5 to 5 mm in diameter.

In vitro binding assay. To evaluate specificity and affinity of conjugates binding assays were carried out as we described recently.[28] Approximately 1×10^6 $PSMA^+$ PC3 PIP and $PSMA^-$ PC3 flu cells were suspended in Flow Cytometry Staining (FACS) buffer (PBS, 2 mM EDTA, 0.5% FBS), placed in FACS tubes, followed by addition of conjugates to achieve final concentrations ranging from 1 nM to 0.64 µM. Incubation with gentle rocking continued for 60 min at RT. Cells were then washed three times with 1 mL of cold PBS, transferred to a 96-well plate and fluorescence with excitation at 775 nm and emission at 800 nm was read using a Synergy™ 2 Multi-Mode Microplate Reader (Winooski, VT). To derive K_d values, the binding isotherms were fitted to a one-site binding hyperbola using GraphPad Prism 4 software (GraphPad Software, Inc., San Diego, CA). To determine binding specificity, 1 mM of the known PSMA inhibitor ZJ-43 was applied.[31] All experiments were performed in triplicate.

Confocal microscopy. To evaluate *in vitro* uptake of the conjugates in $PSMA^+$ PC3 PIP and $PSMA^-$ PC3 flu cell lines, 2×10^4 cells/$2cm^2$ (500 µL) were seeded in a chamber slide overnight. After 24 h the growth medium was exchanged for 250 µL of fresh medium containing 5 µM of conjugate followed by incubation for 2 h at 37°C. After washing with PBS to remove unbound conjugate, cells were fixed with fresh 4% perfluoroalkoxy polymer (PFA) for 10 min and cell nuclei were stained with 5 µM DAPI. Fluorescence microscopy (Olympus IX81, Center Valley, PA) was performed with data processed using ImageJ software.

Optical imaging. The *in vivo* PSMA specificity of conjugates **I - VI** was evaluated in male NOD-SCID mice bearing $PSMA^+$ PC3 PIP and $PSMA^-$ PC3 flu xenografts using NIR optical imaging. The dose of conjugates injected to the tail vain was adjusted to administer the same number of moles (22.3 nmol) of Cy7.5 dye. The following doses of conjugates were administered: 34.38 µg (22.3 nmol) of **I**, 244 µg (11.12 nmol) of **II**, 133 µg (5.59 nmol) of **III**, 100 µg (3.72 nmol) and 200 µg

(7.56 nmol) of **IV**, 85 µg (2.79 nmol) of **V** and 85 µg (3.72 nmol) of **VI**, (n = 3-5). Mice were anaesthetized with isoflurane and serial images of the dorsal, left lateral, ventral and right lateral surfaces were captured using the LI-COR Pearl Impulse Imager (Lincoln, NE) in white light and 800 nm channels (Software v2.0, LI-COR Biosciences) at 5, 24, 48 and 72 h after injection (ai). Upon completion of imaging studies, mice were euthanized, and tumors and selected tissues were dissected, imaged *ex vivo* and stored at -80°C embedded in optimal cutting temperature (OCT) compound for further evaluation. To quantify signal, regions of interest (ROIs) were drawn around tumors and tissues. Mean signal intensity in each ROI was normalized by subtracting the background signal (ROI outside tissues) and used for statistical analysis. Data are shown as mean fluorescence intensity values ± SEM. To assess accumulation of the conjugates in $PSMA^+$ PC3 PIP and $PSMA^-$ PC3 flu tumors and kidneys, tissues frozen in OCT were cut at a 50 µm thickness using a cryomicrotome (ThermoFisher, Rockville, MD). Sections were subsequently viewed on a LI-COR Odyssey imaging system (Lincoln, NE). The sections were fixed with freshly prepared 4% PFA in PBS (pH 7.4) for 15 min prior to immunofluorescence. Before incubation with primary antibodies, non-specific binding was blocked with 10% normal goat serum and 0.1% Triton X-100 for 60 min. To image blood vessels, the primary anti-collagen IV (Abcam, ab6586) antibody was applied and incubated overnight at 4°C. After rinsing with PBS, the sections were exposed to goat anti-rabbit (Alexa Fluor 488, green, Santa Cruze, Dallas, TX) secondary antibody, for 60 min at RT, and cell nuclei were stained with 5 µM DAPI. A fluorescence microscope (Olympus IX81, Center Valley, PA) was used to obtain images.

Photoacoustic/ultrasound imaging system. Real-time PA/US recording, data acquisition, beamforming and all post-processing were implemented on a Vantage 256 ultrasound research system (Verasonics Inc., Kirkland, WA). The sampling frequency (20.83 MHz) was 4 times the central frequency (5.208 MHz) of the linear array transducer (L7-4; 128 elements at 0.3 mm pitch), which has an elevational focusing at 2 cm depth. The tunable wavelength range of the optical parametric oscillator (OPO) system has a resolution of 1 nm interval step, and pulse duration of 5 ns. The generated laser pulse was split by a beam splitter, where 10% of the energy was measured by a pulse energy meter from Ophir Optronics (Jerusalem, Israel), enabling pulse-to-pulse compensation of energy variation. The remaining 90% of the energy was used for PA imaging and delivered through customized bifurcated fiber optic bundles co-registered to the US array transducer, in which each side has a 40 mm long and 0.88 mm wide aperture for uniform energy distribution across the cross-sectional image. The light delivery through the fiber bundle was focused at an imaging depth of 2 cm to be aligned with the elevational acoustic lens focusing of the transducer. For both tubing phantom and *in vivo* experiments the laser was tuned from 700 nm to 900 nm with 10 nm steps, and 64 frames recorded at each wavelength for averaging. B-mode US images were concurrently recorded along with PA images to provide anatomic information in *in vivo* tumor models. All US and PA images were acquired sequentially at 20 Hz using the same L7-4 transducer, enabling accurate co-registration of the two modalities. Image overlay was implemented on RGB images using Daubechies 2 wavelet transform in the MATLAB software (Mathworks Inc., Natick MA).

Photoacoustic characterization of conjugates. PA spectral characteistics of all conjugates were evaluated using the tubing phantom, where medical grade tubes (0.050" ID x 0.090" OD Tygon® ND 100-80 Microbore Tubing, United States Plastic Corporation) were straightened and fixed in parallel in 1 cm intervals in the lateral direction in a water tank at an axial depth of 2 cm. Note that the conjugate samples were prepared in 200 µL of deionized water or PBS containing 9.6 nmol sulfo-Cy7.5. Samples were injected into the tubing phantom. A cross section of the tube was imaged and the PA intensity within the tubing region was averaged to represent the PA datapoint at the corresponding wavelength.

In vivo multi-spectral photoacoustic and ultrasound imaging of PC. Mice used in fluorescence imaging were also imaged in the dorsal position using PA imaging, where $PSMA^+$ PC3 PIP xenografts were in the right and $PSMA^-$ PC3 flu xenografts were in the left lateral flanks. During the imaging procedure at pre- and post-injection (0, 5, 24, 48, and 72 h time points), mice were anaesthetized with isoflurane and placed on a fixation stage. Hair was removed from xenograft regions, which were covered with acoustic gel. Note that the centers of the tumors were selected as ROIs and centered to the elevational focal point of the array (i.e., 2 cm), guided by B-mode US imaging. A least-squares spectral decomposition algorithm was applied using a computational workstation off-line to decompose the concentration of the dendrimer conjugate. That spectral decomposition algorithm was based on our previously published approach,[25] where the PA effect in hemoglobin, deoxyhemoglobin, and the PSMA imaging agent were assumed linearly independent from each other.

Conjugate signal quantification and analysis. In both phantom and *in vivo* experiments the ROIs were centered to a depth of approximately 2 cm within the PA images, the elevational focal depth of laser excitation and acoustic focusing. To obtain two-dimensional (axial and lateral) spatial PA images of each material (conjugates, Hb and HbO_2), the acquired three-dimensional (axial, lateral, and spectral) multispectral PA volumes were decomposed pixelwise using a linear spectral unmixing model given as:

$$\boldsymbol{y} = \Gamma \mathrm{F} \sum_{i=1}^{N} \boldsymbol{\mu} x_i$$

$$x_i \geq 0, \forall i$$

where $\boldsymbol{y} \in \mathbb{R}^M$ is the multispectral photoacoustic signal, $M \in \mathbb{R}$ is the total number of wavelengths, $N \in \mathbb{R}$ is the total

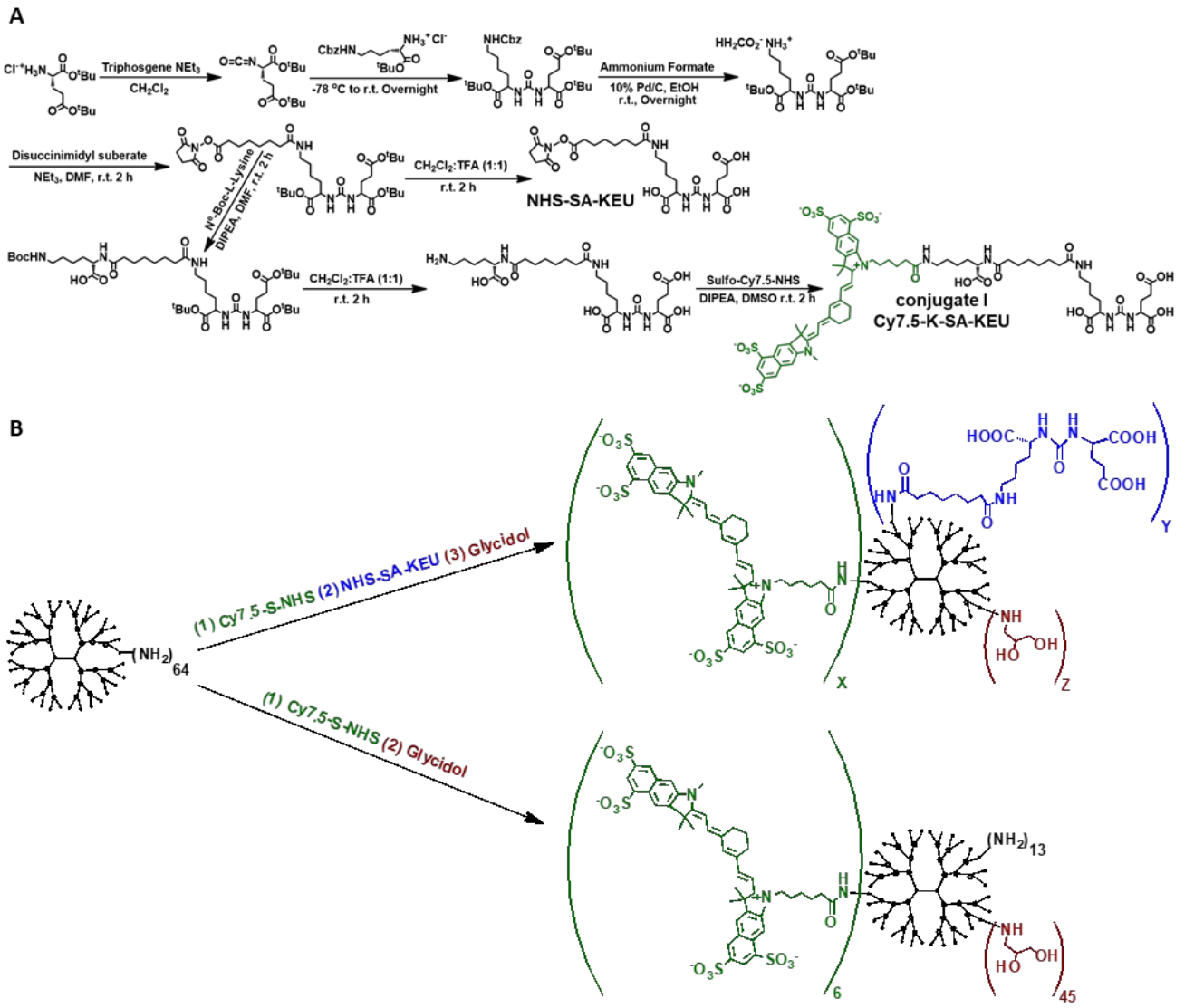

number of tissue types, $\Gamma \in \mathbb{R}$ is the Grüneisen parameter, $F \in \mathbb{R}$ is the optical fluence, $\boldsymbol{\mu} \in \mathbb{R}^M$ is the molar extinction coefficient, and $x \in \mathbb{R}$ is the unknown concentration. In this work both Γ and F are assumed homogeneous. For quantitative analysis, ROIs around the center of xenografts were manually segmented based on the overlaid US image and the PA image at 780 nm, where superficial xenograft regions were avoided to preclude potential acoustic scattering artifacts generated by air bubbles in the acoustic coupling material. To compare conjugate effectiveness, the average PA intensity of $PSMA^+$ PC3 PIP and $PSMA^-$ PC3 flu of the mouse at 0 h was taken as the baseline, then spectral unmixed conjugate maps at all-time points (0, 24, 48, 72 h) were normalized with respect to this baseline.

3. Results

3.1. Synthesis and physicochemical characterization

The synthesis of the NHS-SA-KEU low-molecular-weight PSMA targeting moiety for conjugation with dendrimer, and synthesis of the Cy7.5-K-SA-KEU imaging agent are shown in Figure 1A. Protected Glu-Lys-urea (KEU) was synthetized as previously reported.[29] Protected SA-KEU was then reacted with commercially available DSS to afford the NHS ester

Figure 1A - Synthesis of the PSMA-targeting moiety NHS-SA-KEU (*N*-hydroxysuccinimide ester-suberic acid-lysine-glutamate-urea) for conjugation with dendrimer and PSMA-targeted Cy7.5-K-SA-KEU **conjugate I** (sulfo-cyanine7.5-lysine-suberic acid-lysine-glutamate-urea); **B** - Scheme demonstrating formulation of PSMA-targeted dendrimers (**conjugate II** - generation 4 PAMAM dendrimer conjugated with 2 Cy7.5 dyes, 10 SA-KEU targeting agents and capped with 32 butane-1,2-diol moieties; **conjugate III** - generation 4 PAMAM dendrimer conjugated with 4 Cy7.5 dyes, 9 SA-KEU targeting agents and capped with 30 butane-1,2-diol moieties; **conjugate IV** - generation 4 PAMAM dendrimer conjugated with 6 Cy7.5 dyes, 9 SA-KEU targeting agents and capped with 53 butane-1,2-diol moieties; **conjugate V** - generation 4 PAMAM dendrimer conjugated with 8 Cy7.5 dyes, 12 SA-KEU targeting agents and capped with 52 butane-1,2-diol moieties); and, **conjugate VI** (non-

targeted control - generation 4 PAMAM dendrimer conjugated with 6 Cy7.5 dyes and capped with 52 butane-1,2-diol moieties).

	# of Cy7.5	# of SA-KEU	# of Bdiol	MW (Da)	Size (nm)	ZP (mV)	QR_{780} (%)	RPA_{max} (%)	RPA (%)	K_d (μM)
I	1	1	0	1,554	N/A	N/A	N/A	N/A	N/A	0.78
II	2	10	32	21,950	4.8 ±2.8	-3.4 ±1.9	76.4	30.8	30.3	0.68
III	4	9	30	23,800	5.5 ±2.2	-3.2 ±1.8	174.9	20.9	20.6	0.27
IV	6	9	53	26,954	4.6 ±1.7	-7.2±1.1	4.4	49.0	48.1	0.41
V	8	12	52	30,400	5.2 ±1.9	-10.8 ±0.6	1.3	97.5	111.1	0.078
VI	6	0	45	22,590	3.9 ±2.5	-4.9 ±1.8	26.6	45.4	44.6	N/A

Cy7.5 - sulfo-cyanine7.5, SA-KEU - suberic acid-lysine-glutamate-urea, Bdiol - butane-1,2-diol, MW - molecular weight as measured by MALDI-TOF, ZP - zeta potential, QR - quenching rate, RPA_{780} - ratio of photoacoustic intensity at 780 nm, RPA_{max} - ratio of maximum PA intensity in NIR range, K_d - dissociation constant, N/A - not-applicable.

Table 1. Characteristics of conjugates

derivative, followed by removal of the *tert*-butyl protecting groups to give NHS-SA-KEU. NHS-SA-KEU was purified with RP flash chromatography, lyophilized, characterized by LC-MS (Figure S1) and further used for the synthesis of conjugates **I, II, III, IV** and **V**. Conjugate **I** was prepared according to a method described for our previously reported NIR imaging agent, YC-27, however Cy7.5 was used in place of IR800CW.[14, 25] NHS-SA-KEU was reacted with N^{ε}-Boc-L-Lysine, followed by removal of Boc and *tert*-butyl protecting groups and conjugation of Cy7.5 (Figure 1A). Conjugate **I** Cy7.5-K-SA-KEU was purified by RP-HPLC (Figure S2A). MALDI-TOF mass spectrometry confirmed its identity, with a molecular weight of 1,554 Da (Figure S2B).

PSMA-targeted dendrimer conjugates were assembled using a one-pot synthesis *via* consecutive conjugation of Cy7.5 NIR dyes, SA-KEU PSMA targeting moieties and capping of the remaining terminal primary amine groups with butane-1,2-diol moieties, as presented in Figure 1B. The average number of conjugated functionalities was determined based on an increase of the molecular weight upon each synthetic step, as measured by MALDI-TOF mass spectrometry (Figure 2A). We synthetized four PSMA-targeted dendrimer conjugates having on average 2, 4, 6, and 8 Cy7.5 dyes and from 9 to 12 SA-KEU targeting moieties and terminal butane-1,2-diol functionalities. The non-targeted control dendrimer conjugate was formulated by conjugating 6 sulfo-Cy7.5 dyes and capping the remaining primary amines with butane-1,2-diol functionalities. All conjugates were analyzed by RP-HPLC to assess their purity and confirm covalent attachment of Cy7.5 dyes with dendrimer, as demonstrated by the UV-Vis spectra recorded under the peak of the chromatogram (Figure 2B, S4). DLS analysis indicated similar size distribution for all dendrimer conjugates averaging around 5 nm and zeta potential analysis revealed their negative surface charge (Table 1 and Figure S6). Spectrophotometric, spectrofluorometric and PA properties of all conjugates are demonstrated in Figure 2 C-F and physicochemical properties of all conjugates are collected in Table 1. Figure 2C shows the absorbance spectra of all conjugates formulated into 600 μL samples containing 2.88 nmol Cy7.5 dye. Each sample was equally split into three for spectrophotometric, spectrofluorometric, and PA evaluation, respectively. To obtain the excitation wavelength for fluorescence evaluation as well as estimating the shape of the PA spectra, optical absorbances of all conjugates were first collected on the spectrophotometer in the range from 650 nm to 950 nm in steps of 1 nm. When the total amount of the conjugated Cy7.5 dye remained invariant, the maximum optical absorbance of conjugates **II**, **III**, **IV**, **V**, and **VI** were 24.4% (781 nm), 14.8% (780 nm), 32.3% (781 nm), 55.5% (778 nm), and 26.3% (781 nm) of the maximum optical absorbance of conjugate **I** (779 nm), respectively.

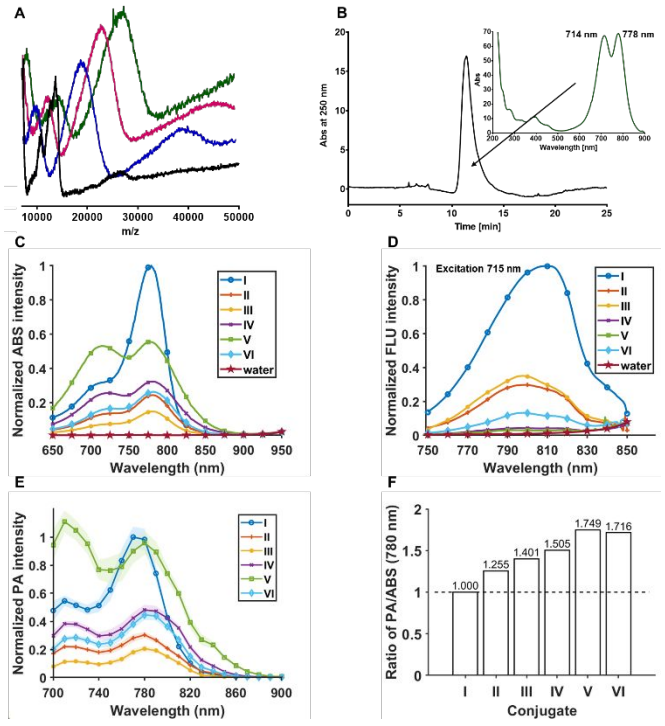

Figure 2. Physicochemical characterization. A - Representative MALDI-TOF MS spectra illustrating an increase of the molecular weight upon each modification

step of the generation 4 amine terminated PAMAM dendrimer [1 - G4(NH_2)$_{64}$, MW=13,115 Da]. Consecutive conjugates were obtained through conjugation of six Cy7.5 dyes [2 - G4(NH_2)$_{58}$(Cy7.5)$_6$, MW=18,397 Da], nine SA-KEU targeting agents [3 - G4(NH_2)$_{49}$(Cy7.5)$_6$(SA-KEU)$_9$, MW=23,013 Da] and capping of the remaining primary amines with butane-1,2-diol moieties [4 - G4(Cy7.5)$_6$(SA-KEU)$_9$(Bdiol)$_{53}$, MW=26,954 Da final PSMA-targeted dendrimer conjugate **IV**]; **B -** RP-HPLC chromatogram of conjugate **IV** with the UV-Vis spectrum recorded under the peak, indicating covalent attachment of Cy7.5 to the dendrimer; **C -** Spectrophotometric properties of all conjugates and purified water from 650 nm to 950 nm in steps of 1 nm; **D** - Spectrofluorometric properties of all conjugates and purified water. Excitation was at 715 nm and emission was from 750 nm to 850 nm in steps of 1 nm; **E** - PA properties of all conjugates from 700 nm to 900 nm in steps of 10 nm; **F** - Ratio of PA intensity to absorbance at 780 nm of all conjugates. From **C** to **F** all intensities were normalized with respective to conjugate **I**.

In the range of 750 - 800 nm, low-molecular-weight conjugate **I** displayed higher absorbance than did the dendrimer conjugates, but all dendrimer conjugates demonstrated higher absorbance values than conjugate **I** in the longer wavelength range (> 800 nm). Below 750 nm, conjugate **V** showed a higher absorbance than conjugate **I**, reaching the highest fold change of 1.8× at 678 nm. Spectrofluorometric evaluation was performed between 750 nm and 850 nm with excitation at 715 nm in steps of 1 nm. The normalized fluorescence intensity spectra are demonstrated in Figure 2D and the quenching rates are included in Table 1. Because of the fluorescence quenching, a higher portion of optical energy was converted to thermal energy so that thermal-elastic expansion was amplified, as indicated in Figure 2E. As listed in Table 1, the ratio of PA intensities of conjugates **II**, **III**, **IV**, **V**, and **VI** vs conjugate **I** at 780 nm were 30.8%, 20.9%, 49.0%, 97.5%, and 45.4%, respectively. However, conjugates **II**, **III**, **IV**, **V**, and **VI** presented 125.5%, 140.1%, 150.5%, 174.9% and 71.6% of fractional PA signal when normalized to the given absorbance at 780 nm (Figure 2F), respectively.

3.2. In vitro evaluation

To assess the affinity and specificity of the conjugates to PSMA *in vitro*, we carried out binding assays using the isogenic human prostate cancer cell lines, PSMA$^+$ PC3 PIP and PSMA PC3 flu.[30] Figure 3 displays representative results obtained for conjugate **IV**, which showed significantly higher accumulation in PSMA$^+$ PC3 PIP cells compared with PSMA$^-$ PC3 flu cells (Figure 3A). An excess of ZJ-43, a known small-molecule PSMA inhibitor,[31] decreased the uptake of conjugate **IV** by PSMA$^+$ PC3 PIP cells, confirming binding specificity. Conjugate **IV** also showed a concentration-dependent increase of fluorescence intensity upon elevation of its concentration in PSMA$^+$ PC3 PIP cells (Figure 3B) with a

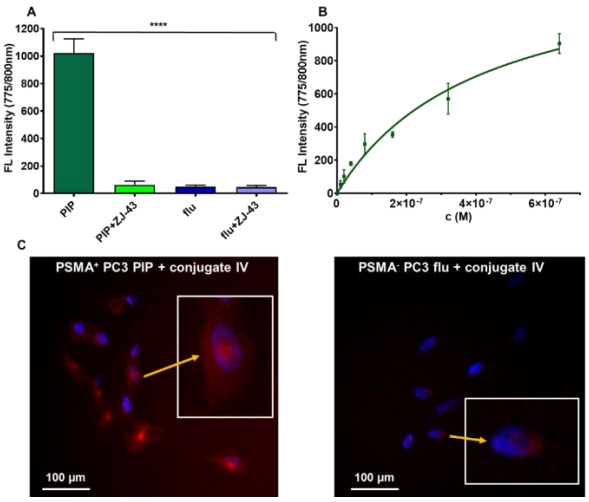

Figure 3. ***In vitro*** **evaluation of conjugate IV. A -** Conjugate **IV** binding to PSMA$^+$ PC3 PIP and PSMA$^-$ PC3 flu cell lines (each cell type was incubated with conjugate **IV** in the presence or absence of the known PSMA inhibitor ZJ-43, followed by washing and analysis on a plate reader,**** $P < 0.001$); **B** - Representative curve of conjugate **IV** binding to PSMA$^+$ PC3 PIP; **C** - Microscopic evaluation of conjugate **IV** uptake by PSMA$^+$ PC3 PIP and PSMA$^-$ PC3 flu cell lines (blue - cell nuclei stained with DAPI and red - conjugate **IV**). Data demonstrate high *in vitro* PSMA-binding specificity of conjugate **IV**.

derived K_d value of 0.41 µM (95% confidence interval 0.16 - 0.66 µM). Conjugate **IV** also showed significantly higher internalization in PSMA$^+$ PC 3 PIP cells compared with PSMA$^-$ PC3 flu cells as demonstrated by microscopy (Figure 3C). Similar results were obtained for other conjugates, with derived K_d values presented in Table 1.

3.3. In vivo evaluation

All conjugates retained fluorescence intensity that enabled their detection in NOD-SCID mice bearing subcutaneous PSMA$^+$ PC3 PIP and PSMA$^-$ PC3 flu xenografts by NIR imaging (Figures 4, 5, S9 and S10). Conjugate **IV** demonstrated the highest *in vivo* PSMA binding specificity with PSMA$^+$ PC3 PIP/PSMA$^-$ PC3 flu tumors ratio of 6.2 ± 1.2 and lowest off-target tissue uptake (Figure 4). Whole-body imaging indicated specific accumulation of conjugate **IV** in PSMA$^+$ PC3 PIP tumors at 5 h ai. At the same time point fluorescence could also be detected in kidneys and bladder (Figure 4, dorsal image). At 24, 48 and 72 h after injection, conjugate **IV** could be detected only in PSMA$^+$ PC3 PIP tumors. *Ex vivo* evaluation of dissected tissues confirmed the highest fluorescence intensity in targeted tumors.

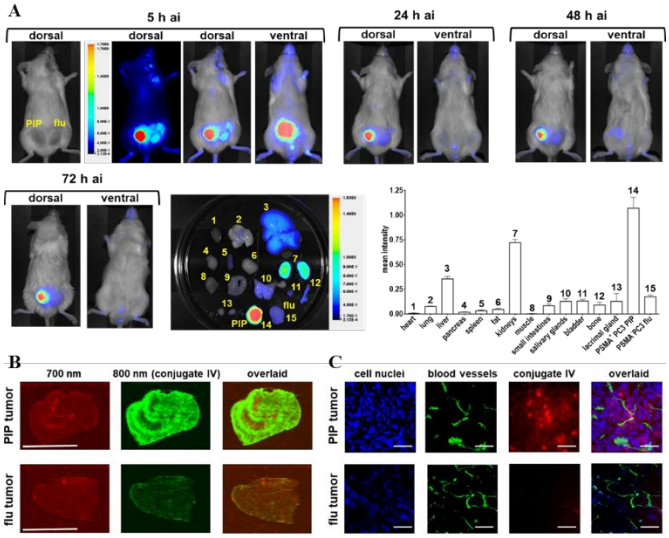

Figure 4. FL evaluation of conjugate IV. A - NOD-SCID mice bearing subcutaneous PSMA$^+$ PC3 PIP and PSMA$^-$ PC3 flu in the lower back near left and right posterior flanks, respectively, were injected with conjugate **IV**, and images were acquired in the visible and NIR (excitation 785 and emission 820 nm) channels at 5, 24, 48 and 72 h ai. Representative image of conjugate **IV** biodistribution at 72 h ai and semi-quantitative analysis of fluorescence intensity (column numbers in the graph represent the tissue numbers, n=5); **B -** Conjugate **IV** uptake in dissected PSMA$^+$ PC3 PIP and PSMA$^-$ PC3 tumors. Images were collected using 700 nm (excitation 685 and emission 730 nm, red) and 800 nm (excitation 785 and emission 830 nm green) channels, scale bar denotes 5 mm; **C -** Conjugate **IV** in PSMA$^+$ PC3 PIP and PSMA$^-$ PC3 tumors at the microscopic level (blue - cell nuclei stained with DAPI, green - blood vessels visualized using collagen, red - conjugate **IV**, bar denotes 120 µm). Data indicate preferential accumulation of the conjugate **IV** in PSMA$^+$ PC3 PIP tumors vs. other tissues and extravasation from blood vessel.

Relatively lower fluorescence signal could also be detected in kidneys, followed by liver. Evaluation of tumor sections revealed presence of conjugate **IV** in the entire volume of PSMA$^+$ PC3 PIP tumors (Figure 4B and S7). Microscopic studies involving staining of blood vessels (green) and cell nuclei (blue) indicated extravasation of conjugate **IV** (red) and cellular internalization (Figure 4C) within PSMA$^+$ PC3 PIP tumors. Microscopic imaging of kidney samples revealed presence of conjugate **IV** in proximal convoluted tubules (Figure S8). As expected, significantly lower accumulation of conjugate **IV** was observed in sections of PSMA$^-$ PC3 flu tumors (Figure 4B and S7). All other PSMA$^+$ targeted dendrimer conjugates **II**, **III** and **V** showed lower PSMA$^+$ PC3 PIP/PSMA$^-$ PC3 flu tumors ratios than conjugate **IV**, with values of 3.1 ± 1.0, 3.0 ± 1.0 and 3.7 ± 1.3, respectively, as well as relatively higher kidney and liver uptake (Figures 4 and S9). In contrast to PSMA-targeted conjugates, non-targeted control conjugate **VI** did not show preferential uptake in PSMA$^+$ tumors, demonstrating a PSMA$^+$ PC3 PIP/PSMA$^-$ PC3 flu tumors ratio of 1.0 ± 0.1, with predominant accumulation in kidneys followed by salivary glands and liver (Figure S9). To compare *in vivo* PSMA targeting and optical properties of dendrimer conjugates with low-molecular-weight conjugate **I**, we next evaluated conjugate **I** in the same mouse tumor model as for the dendrimers (Figure 5). As expected, after administration of the same molar amount of Cy7.5 as for the dendrimer conjugates, optical imaging showed significantly higher fluorescence intensity *in vivo* and *ex vivo*, due to the lack of fluorescence quenching, which was observed for conjugates **II**, **III**, **IV**, **V** and **VI**, shown in Figure 2.

Conjugate **I** also showed preferential accumulation in PSMA$^+$ tumors with PSMA$^+$ PC3 PIP/PSMA$^-$ PC3 flu tumors ratio of 3.1 ± 0.8, however its highest uptake was detected in kidneys followed by liver. Preferential accumulation of conjugate **I** in PSMA$^+$ tumors appeared lower than for conjugate **IV**, with a PSMA$^+$ PC3 PIP/PSMA$^-$ PC3 flu tumors ratio of 6.2 ± 1.2.

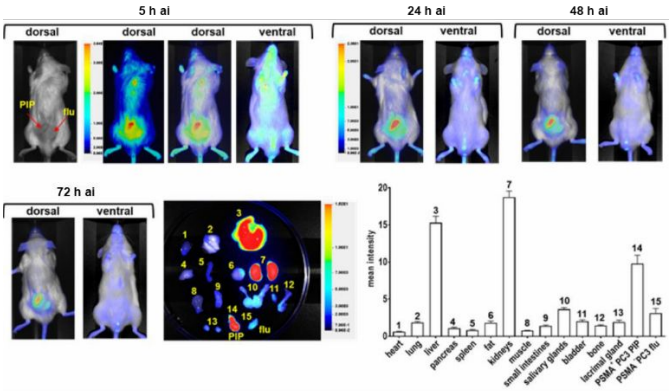

Figure 5. NIR FL imaging of conjugate I. NOD-SCID mice bearing subcutaneous PSMA$^+$ PC3 PIP and PSMA$^-$ PC3 flu in the lower back near left and right posterior flanks, respectively, were injected with conjugate **I** and images were acquired in the visible and NIR (excitation 785 and emission 820 nm) channels at 5, 24, 48 and 72 h ai. Representative image of the biodistribution of conjugate **I** at 72 h ai and semi-quantitative analysis of fluorescence intensity (column numbers in the graph represent the tissue numbers, n=5). Data indicate preferential uptake of conjugate **I** (low molecular weight Cy7.5-K-SA-KEU) in PSMA$^+$ PC3 PIP tumors vs. PSMA$^-$ PC3 flu tumors with its relatively high uptake in kidneys and liver.

Conjugate **I** also showed preferential accumulation in PSMA$^+$ tumors with PSMA$^+$ PC3 PIP/PSMA$^-$ PC3 flu tumors ratio of 3.1 ± 0.8, however its highest uptake was detected in kidneys followed by liver. Preferential accumulation of conjugate **I** in PSMA$^+$ tumors appeared lower than for conjugate **IV**, with a PSMA$^+$ PC3 PIP/PSMA$^-$ PC3 flu tumors ratio of 6.2 ± 1.2.

After confirmation of PSMA-targeted specificity of the conjugates *in vivo* with NIR FL imaging, we carried out PA imaging using the same mice. Figure 6 demonstrates *in vivo*

PA imaging of low-molecular-weight conjugate **I**, PSMA-targeted dendrimer conjugate **IV** and non-targeted control dendrimer conjugate **VI**. Figure 6A depicts representative US images, where tumor boundaries are enclosed by white dotted lines. In all images, PSMA$^-$ PC3 flu tumors are consistently to the left of PSMA$^+$ PC3 PIP tumors.

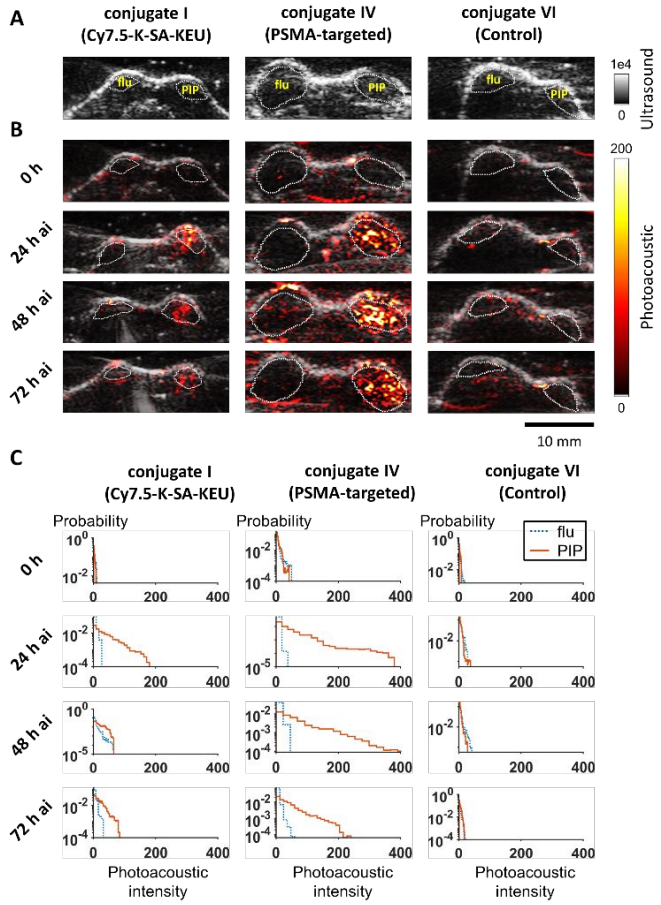

Figure 6. Ultrasound and photoacoustic imaging. A - US imaging with delineation of PSMA$^+$ PC3 PIP and PSMA$^-$ PC3 flu tumors; **B** - Overlaid US and PA imaging showing accumulation of low molecular weight conjugate **I** in PSMA$^+$ PC3 PIP and PSMA$^-$ PC3 flu tumors, PSMA-targeted dendrimer conjugate **IV**, and non-targeted control dendrimer conjugate **VI**. The same mice were imaged by both FL and US/PA imaging. US/PA Images were collected using an Nd:YAG OPO laser and Verasonics Vantage 256 ultrasound research platform before injection of the conjugates and 24, 48, and 72 h ai once the conjugates accumulated in PSMA$^+$ PC3 PIP and PSMA$^-$ PC3 flu tumors. Data indicate that the conjugates **I** and **IV** could be used for detection of PSMA expression in PMSA$^+$ PC3 PIP. **C** - Histogram of normalized PA intensities that are greater than 1 (the baseline) in the ROIs of PSMA$^+$ PC3 PIP and PSMA$^-$ PC3 flu tumors.

Figure 6B demonstrates the spectral decomposition contrast provided by each conjugate. In visual assessment, conjugates **I** and **IV** showed preferential accumulation in PSMA$^+$ PC3 PIP tumors. Figure 6C presents PA intensity histograms in tumor regions corresponding to the images in Figure 6B. Only intensities greater than the baseline value (greater than 1 after normalization) were included in the histogram. Results obtained for PSMA$^+$ PC3 PIP and PSMA$^-$ PC3 flu tumors are presented in red solid lines and blue dotted lines, respectively. Figure 6C showed that PA intensity in tumor regions follows exponential distribution. Before injection of conjugates, there was minimal PA signal in PSMA$^+$ PC3 PIP and PSMA$^-$ PC3 flu tumors. In agreement with NIR FL imaging, conjugate **I** and **IV** showed significantly higher PA contrast in PSMA$^+$ PC3 PIP tumors than in PSMA$^-$ PC3 flu tumors with consistently stronger PA signal for dendrimer conjugate **IV.** Lack of PA contrast in PSMA$^+$ PC3 PIP and PSMA$^-$ PC3 flu tumors observed for non-targeted control conjugate **VI** further supported the PSMA specificity of conjugate **IV.**

Figure 7 presents the relative changes in signal intensities due to conjugates **I**, **IV** and **VI**, decomposed in PSMA$^+$ PC3 PIP and PSMA$^-$ PC3 flu xenografts with respect to the baseline recorded prior to their administration. For conjugate **IV**, the measured PA intensities of the decomposed PAMAM conjugate maps within the ROIs of PSMA$^+$ PC3 PIP were 1.1 ± 0.4, 25.1 ± 11.0, 30.2 ± 21.1, and 21.8 ± 7.4 (a.u., arbitrary unit) before injection and at 24, 48 and 72 h ai, respectively. At the same time points, the corresponding PA intensities within the ROI of PSMA$^-$ PC3 flu tumors were 0.9 ± 0.4, 4.2 ± 4.3, 5.9 ± 2.5, 3.8 ± 1.3 (a.u.). For the non-targeted control dendrimer conjugate **VI**, in agreement with the fluorescence imaging results, there was minimal PA signal in either tumor model. The measured PA image intensities of the decomposed conjugate **IV** maps within the ROI in PSMA$^+$ PC3 PIP tumors were 1.1 ± 0.2, 1.1 ± 0.9, 3.8 ± 4.1, and 1.6 ± 1.4 (a.u.) pre-injection and at 24, 48 and 72 h ai, respectively. The corresponding PA intensities within the ROI in PSMA$^-$ PC3 flu tumors were 0.9 ± 0.4, 2.0 ± 0.9, 3.4 ± 2.4, and 0.9 ± 0.7 (a.u.). Further, selective accumulation of conjugate **I** in PSMA$^+$ PC3 PIP tumors vs. PSMA$^-$ PC3 flu could be also detected from the PA images (Figure 6B). In particular, the measured PA signal intensities of the decomposed conjugate **I** maps within the ROI of PSMA$^+$ PC3 PIP tumors were 0.8 ± 0.3, 21.6 ± 16.8, 12.7 ± 5.2, and 10.0 ± 4.8 (a.u.) pre-injection and at 24, 48 and 72 h ai, respectively. The corresponding average PA signal intensities within the ROI of PSMA$^-$ PC3 flu were 1.4 ± 0.5, 1.9 ± 1.4, 19 ± 0.9, and 2.0 ± 1.1 (a.u.). Overall, with PA imaging the decomposed intensity of both conjugate **I** and conjugate **IV** revealed their preferential accumulation in PSMA$^+$ PC3 PIP tumors vs. PSMA$^-$ PC3 flu tumors throughout all evaluated time points (n = 5 each): P = 0.0312, 0.0018, and 0.0067 at 24, 48, and 72 h ai for conjugate **I**; and P = 0.0042, 0.0343, and 0.0007 at 24, 48, and 72 h after ai for conjugate **IV**. In contrast, control conjugate **VI** indicated no statistical significance of decomposed dye intensities between tumors with P = 0.1769 (not significant, n.s.), 0.8797 (n.s.), and 0.5853 (n.s.) at 24, 48, and 72 h ai, respectively.

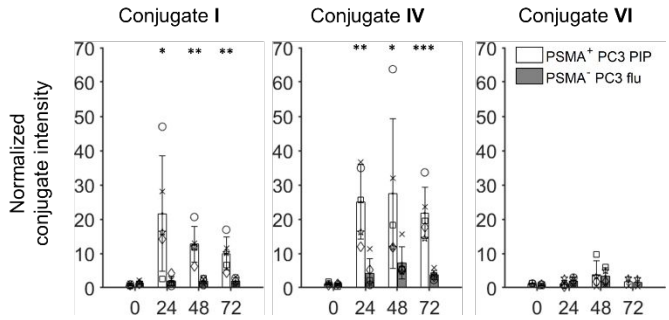

Figure 7. **PA contrast of conjugates.** Bar chart of the change in contrast over time for each conjugate. Data points from different mice are indicated by different markers. Three, two, and one asterisks correspond to *P*-values < 0.001, < 0.01, and < 0.05, respectively.

4. Discussion

The aim of this study was to synthesize PSMA-targeted PAMAM dendrimer conjugates as contrast agents for FL and PA imaging and to test them in experimental models of PC. We recently demonstrated that a generation 4 PAMAM dendrimer conjugated with DOTA, rhodamine, MP-KEU (5-mercapto-pentanamide-lysine-glutamate-urea) and butane-1,2-diol terminal moieties had pharmacokinetics suitable for targeting PSMA$^+$ tumors with imaging or therapeutic agents.[28] Conjugation of six Cy7.5 dyes to a PSMA-targeted generation-4 PAMAM dendrimer provided a dual FL and PA imaging contrast agent, conjugate **IV**. To streamline synthesis of the PSMA-targeted dendrimer conjugates, we used an *N*-hydroxysuccinimide ester-activated NHS-SA-KEU PSMA targeting moiety and circumvented application of a succinimidyl-4-[*N*-maleimidomethyl]cyclohexane-1-carboxylate (SMCC) heterobifunctional linker. That approach facilitated control over the number of PSMA-targeting moieties conjugated with dendrimer and leads to more reproducible synthesis of conjugates with less substitutional imperfections.[32] We focused our effort on PAMAM dendrimers because their pharmacokinetic and signal characteristics can be more readily tuned in contrast to previously published Y-27 and conjugate **I**. For example, because amplification of the PA signal is possible with the dendrimers, we can attach multiple functionalities and can use dyes that more readily enable photothermal therapy. Dendrimers can also be fashioned with drugs attached to their surface, or, if lipophilic, within their core.[26] Furthermore, PAMAM dendrimers have a number of advantages compared to relatively larger nanoparticles or antibodies, including enhanced tunability, solubility, permeability, swift cellular uptake and modifiable pharmacokinetics.[26, 27, 33] Spectrophotometric properties of the PAMAM dendrimer conjugates in the NIR band indicated an increase of absorbance at a higher quenching rate as the number of conjugated Cy7.5 NIR dyes increased. That was because the multi-scaffold Cy7.5 molecules, which are in close proximity, enable energy transfer within the ground state complex. Upon laser excitation, energy absorbed at the shared ground state across multiple dye molecules will contribute to internal conversion rather than fluorescence emission, so that non-radiative relaxation will be intensified in the form of thermal energy, which triggers PA signal amplification. Among all conjugates, **IV** presented both nonlinear amplification of PA effect up to 50.5% from the given absorbance (Figure 2) and preferential accumulation in PSMA$^+$ PC3 PIP tumors with the lowest off-target tissue uptake. As expected, conjugate **IV** showed lower signal intensity in PSMA$^+$ PC3 PIP tumors than conjugate **I** in NIR FL imaging with superior spectral decomposition contrast, indicating significantly better sensitivity for detection of PSMA expression with PA imaging. Other PAMAM dendrimer conjugates showed off-target tissue uptake dominated by kidneys, liver and salivary glands (Figure S5). Conjugate **IV** also showed lower accumulation in kidneys and liver (relative to PSMA$^+$ PC PIP tumors) than low-molecular-weight conjugate **I**, which displayed PSMA-targeted imaging properties and biodistribution similar to previously reported YC-27, which bears a IR800CW NIR dye.[14] For comparison of the structural features of YC-27 and conjugate **I** see Figure S11.[25] Interestingly, conjugation of IR800CW NIR dyes with PAMAM dendrimer resulted in a strong blue-shift with maximum absorbance at 610 nm, excluding these conjugates from PA imaging applications (Figure S12). For that reason, we utilized Cy7.5, which enabled absorbance in the NIR region of the spectrum, even upon conjugation with PAMAM dendrimer. It is important to highlight that fluorescence quenching in dendrimer structure enhances PA contrast in the high PSMA expression cancer. Fluorescence quenching is a well-established technique in applications of voltage-sensitive dye.[34, 35] In this work we have extended this innovation to cancer imaging and identified, and quantified the reciprocal relationship between FL and PA quantum yields seen with FL quenching dyes.

We have identified and quantified the reciprocal relationship between FL and PA quantum yields seen with FL quenching dyes.[35] PAMAM dendrimers provide a controlled environment for FL quenching and hence amplification of PA signal beyond the conventional absorbance limit. Accordingly, conjugate **V** yielded 16.21% and 17.53% higher nonlinear amplification and optical absorbance than those for conjugate **IV**, respectively, indicating that 36.58% higher PA imaging sensitivity can be achieved. However, conjugate **V** did not provide efficient PSMA-specific contrast *in vivo*, most likely due to lower accumulation in PSMA$^+$ PC3 PIP tumors and higher off-target tissue uptake compared to conjugate **IV**. We hypothesize that further optimization of dendrimer surface properties such as charge, hydrophilicity and number of targeting moieties may allow conjugation of more Cy7.5 dyes to obtain higher absorbance and fluorescence quenching without affecting high accumulation in PSMA$^+$ tumors. Based on a previous spectral unmixing framework,[36] we further optimized the method for PA imaging of dendrimer-based agents. That optimization is beyond the scope of the current

study, and will be reported separately. We will also investigate the optimal wavelength selection for PA imaging of dendrimer conjugates in future work. We envision that the dual contrast agent will provide extended efficacy in all PC diagnostic and treatment phases in pre-, intra-, and post-operative circumstances.

5. Conclusions

We have demonstrated that PAMAM dendrimer-based nanoplatforms, which provide multimodal FL and PA contrast, can be targeted to a specific, relevant cancer-related surface protein *in vivo* and demonstrate image contrast superior to that of a small-molecule analog previously used for this purpose. Also, we have presented a mechanism of fluorescence quenching attributed to the configuration of dyes arrayed upon the PAMAM dendrimer, which preserves the amplitude of the PA effect per mole of dye present.

Author contributions

Wojciech G Lesniak: synthesis of PAMAM dendrimer conjugates and their physicochemical analysis, evaluation, *in vivo* and ex vivo fluorescence imaging, writing - original draft. *Yixuan Wu:* near-infrared spectrophotometry, spectrofluorometry, photoacoustic characterization of conjugates, ultrasound/photoacoustic imaging, data analysis, writing - original draft. Jeeun Kang: ultrasound/photoacoustic imaging, data analysis, review and editing. Srikanth Boinapally: synthesis and characterization of low-molecular-weight Cy7.5-SA-KEU imaging agent and NHS-SA-KEU PSMA-targeting moiety for conjugation with dendrimer, review & editing. Sangeeta Ray Banerjee: conceptualization, methodology, investigation. Ala Lisok: growing and preparation of $PSMA^+$ PC3 PIP and $PSMA^-$ PC3 flu cell lines, preparation of tumor mouse models, assistance with *in vivo* fluorescence imaging, collection of tissue samples. Anna Jablonska: confocal microscopy, fluorescence imaging and data analysis, review and editing. Emad M. Boctor: conception, supervision, funding, reviewing and editing. Martin G. Pomper: conception, supervision, funding, reviewing and editing.

Conflicts of interest

There are no conflicts to declare.

Acknowledgements

This work was funded by CA134675, CA184228, CA183031, EB024495, U.S. DoD CDMRP W81XWH-18-1-0188, and the Commonwealth Foundation.

References

1. Ferlay, J., et al., *Cancer incidence and mortality worldwide: sources, methods and major patterns in GLOBOCAN 2012.* Int J Cancer, 2015. **136**(5): p. E359-86.
2. Chen, R.C., et al., *Active Surveillance for the Management of Localized Prostate Cancer (Cancer Care Ontario Guideline): American Society of Clinical Oncology Clinical Practice Guideline Endorsement.* J Clin Oncol, 2016. **34**(18): p. 2182-90.
3. Damodaran, S., J.M. Lang, and D.F. Jarrard, *Targeting Metastatic Hormone Sensitive Prostate Cancer: Chemohormonal Therapy and New Combinatorial Approaches.* J Urol, 2019. **201**(5): p. 876-885.
4. James, N.D., et al., *Failure-Free Survival and Radiotherapy in Patients With Newly Diagnosed Nonmetastatic Prostate Cancer: Data From Patients in the Control Arm of the STAMPEDE Trial.* JAMA Oncol, 2016. **2**(3): p. 348-57.
5. Mamawala, M.M., et al., *Risk prediction tool for grade re-classification in men with favourable-risk prostate cancer on active surveillance.* BJU Int, 2017. **120**(1): p. 25-31.
6. Pinsky, P.F., P.C. Prorok, and B.S. Kramer, *Prostate Cancer Screening - A Perspective on the Current State of the Evidence.* N Engl J Med, 2017. **376**(13): p. 1285-1289.
7. Tosoian, J.J., et al., *Active surveillance program for prostate cancer: an update of the Johns Hopkins experience.* J Clin Oncol, 2011. **29**(16): p. 2185-90.
8. Picchio, M., et al., *Imaging biomarkers in prostate cancer: role of PET/CT and MRI.* Eur J Nucl Med Mol Imaging, 2015. **42**(4): p. 644-55.
9. Kiess, A.P., et al., *Prostate-specific membrane antigen as a target for cancer imaging and therapy.* Quarterly Journal of Nuclear Medicine and Molecular Imaging, 2015. **59**(3): p. 241-268.
10. Maurer, T., et al., *Current use of PSMA - PET in prostate cancer management.* Nature Reviews Urology, 2016. **13**(4): p. 226-235.
11. Phillips, R., et al., *Outcomes of Observation vs Stereotactic Ablative Radiation for Oligometastatic Prostate Cancer: The ORIOLE Phase 2 Randomized Clinical Trial.* JAMA Oncol, 2020.
12. Minner, S., et al., *High level PSMA expression is associated with early PSA recurrence in surgically treated prostate cancer.* Prostate, 2011. **71**(3): p. 281-8.

13. Azad, B.B., et al., *Evaluation of a PSMA-targeted BNF nanoparticle construct.* Nanoscale, 2015. **7**(10): p. 4432-4442.
14. Chen, Y., et al., *A low molecular weight PSMA-based fluorescent imaging agent for cancer.* Biochemical and Biophysical Research Communications, 2009. **390**(3): p. 624-629.
15. Dogra, V., et al., *Photoacoustic imaging with an acoustic lens detects prostate cancer cells labeled with PSMA-targeting near-infrared dye-conjugates.* J Biomed Opt, 2016. **21**(6): p. 66019.
16. Liu, G., et al., *A dextran-based probe for the targeted magnetic resonance imaging of tumours expressing prostate-specific membrane antigen.* Nat Biomed Eng, 2017. **1**: p. 977-982.
17. Pandit-Taskar, N., et al., *Indium 111-labeled J591 anti-PSMA antibody for vascular targeted imaging in progressive solid tumors.* EJNMMI Res, 2015. **5**: p. 28.
18. Fu, Q., et al., *Photoacoustic Imaging: Contrast Agents and Their Biomedical Applications.* Adv Mater, 2019. **31**(6): p. e1805875.
19. Luke, G.P., D. Yeager, and S.Y. Emelianov, *Biomedical applications of photoacoustic imaging with exogenous contrast agents.* Ann Biomed Eng, 2012. **40**(2): p. 422-37.
20. Wang, L.V. and S. Hu, *Photoacoustic tomography: in vivo imaging from organelles to organs.* Science, 2012. **335**(6075): p. 1458-62.
21. Wang, S., et al., *Recent Advances in Photoacoustic Imaging for Deep-Tissue Biomedical Applications.* Theranostics, 2016. **6**(13): p. 2394-2413.
22. Valluru, K.S., K.E. Wilson, and J.K. Willmann, *Photoacoustic Imaging in Oncology: Translational Preclinical and Early Clinical Experience.* Radiology, 2016. **280**(2): p. 332-49.
23. Ju, K.Y., et al., *pH-Induced aggregated melanin nanoparticles for photoacoustic signal amplification.* Nanoscale, 2016. **8**(30): p. 14448-56.
24. Moon, H., et al., *Multifunctional theranostic contrast agent for photoacoustics- and ultrasound-based tumor diagnosis and ultrasound-stimulated local tumor therapy.* J Control Release, 2015. **218**: p. 63-71.
25. Zhang, H.K., et al., *Prostate-specific membrane antigen-targeted photoacoustic imaging of prostate cancer in vivo.* J Biophotonics, 2018. **11**(9): p. e201800021.
26. Araujo, R.V., et al., *New Advances in General Biomedical Applications of PAMAM Dendrimers.* Molecules, 2018. **23**(11).
27. Menjoge, A.R., R.M. Kannan, and D.A. Tomalia, *Dendrimer-based drug and imaging conjugates: design considerations for nanomedical applications.* Drug Discov Today, 2010. **15**(5-6): p. 171-85.
28. Lesniak, W.G., et al., *Evaluation of PSMA-Targeted PAMAM Dendrimer Nanoparticles in a Murine Model of Prostate Cancer.* Mol Pharm, 2019. **16**(6): p. 2590-2604.
29. Maresca, K.P., et al., *A series of halogenated heterodimeric inhibitors of prostate specific membrane antigen (PSMA) as radiolabeled probes for targeting prostate cancer.* J Med Chem, 2009. **52**(2): p. 347-57.
30. Mease, R.C., et al., *N-[N-[(S)-1,3-dicarboxypropyl]carbamoyl]-4-[F-18]fluorobenzyl-L-cysteine, [F-18]DCFBC: A new imaging probe for prostate cancer.* Clinical Cancer Research, 2008. **14**(10): p. 3036-3043.
31. Yamamoto, T., et al., *Antinociceptive effects of N-acetylaspartylglutamate (NAAG) peptidase inhibitors ZJ-11, ZJ-17 and ZJ-43 in the rat formalin test and in the rat neuropathic pain model.* Eur J Neurosci, 2004. **20**(2): p. 483-94.
32. Shi, X., et al., *Generational, skeletal and substitutional diversities in generation one poly(amidoamine) dendrimers.* Polymer, 2005. **46**(9): p. 3022-3034.
33. Wang, T., et al., *Design, Synthesis, and Biological Evaluations of Asymmetric Bow-Tie PAMAM Dendrimer-Based Conjugates for Tumor-Targeted Drug Delivery.* ACS Omega, 2018. **3**(4): p. 3717-3736.
34. Kang, J., et al., *Transcranial Recording of Electrophysiological Neural Activity in the Rodent Brain in vivo Using Functional Photoacoustic Imaging of Near-Infrared Voltage-Sensitive Dye.* Frontiers in Neuroscience, 2019. **13**.
35. Zhang, H.K., et al., *Listening to membrane potential: photoacoustic voltage-sensitive dye recording.* J Biomed Opt, 2017. **22**(4): p. 45006.
36. Wu, Y., et al. *Effective multi-spectral photoacoustic imaging of prostate-specific membrane antigen (PSMA)-targeted agent for aggressive prostate cancer detection," IEEE International Ultrasonics Symposium*. in *IEEE International Ultrasonics Symposium*. 2019.